Titanium-Titanium Boride (Ti-TiB) Functionally Graded Materials through Reaction Sintering: Synthesis, Microstructure, and Properties

K.B. PANDA and K.S. RAVI CHANDRAN

The study demonstrates an effective method to synthesize titanium-titanium boride (Ti-TiB) functionally graded material (FGM) tiles by exploiting the simultaneous TiB whisker formation *in situ* and the densification occurring during the reaction sintering process. The macrostructure of the graded material was designed to have a beta-titanium (β-Ti) layer on one side with the composite layers of Ti-TiB mixture having increasing volume fraction of the TiB through the thickness. The approach used an optimized tri-modal powder mixture consisting of α-Ti powder, a master alloy of the β-stabilizing-element powders (Fe-Mo), and TiB_2. The structure and properties of both of these FGMs were systematically characterized by X-ray diffraction, electron microscopy, and microhardness measurements. Interestingly, it has been found that two different kinds of TiB whisker morphologies were observed in the FGMs. The Ti-rich layers were found to have large and pristine TiB whiskers uniformly distributed in the Ti matrix. On the other hand, the TiB-rich layer was found to have a network of interconnected and relatively smaller TiB whiskers appearing as clusters. The layers of intermediate TiB volume fractions were found to consist of both the morphologies of TiB. The effectiveness of the X-ray direct comparison method for the determination of volume fractions of phases in the FGM layers was also demonstrated. The Vickers microhardness level was found to increase dramatically from 420 kgf/mm^2 in the β-Ti layer to 1600 kgf/mm^2 in the TiB-rich layer. The elastic residual stresses retained in the graded layers after fabrication were determined based on an elastic multilayer model. The nature of microstructure, the hardness variation, and the distribution of residual stresses in these novel FGMs are discussed.

I. INTRODUCTION

A functionally graded material (FGM) is a macroscopically inhomogeneous composite material that has a gradient in composition from one surface to another.[1] Typically, FGMs are made of a metal and a ceramic as opposite faces with the intermediate zones consisting of varying volume fractions of constituents. Originally, the concept of FGMs arose as a result of efforts to prevent the cracking in ceramic-metal joints induced by the coefficient of thermal expansion (CTE) mismatch during high-temperature processing. Direct bonding of the metal and the ceramic generates thermal stresses due to the CTE mismatch and often leads to cracking of the ceramic, thus making the bi-materials unsuitable for structural use.[2] The FGM, on the other hand, has the following advantages over the metal-ceramic joints: (1) effective reduction in the overall magnitude of the thermal stresses,[3] (2) delaying of the plastic yielding and the failure of the metallic layer by the load sharing of the ceramic,[4] and (3) a better overall use of the available materials by distributing them in a suitable spatial direction.

There are also additional benefits that can be gained by adopting FGMs for high-temperature applications. The gradation results in a continuous variation in material properties such as the thermal expansion coefficient and the elastic modulus, which can lead to improvements in thermal shock resistance and toughness. The concept of FGM was initially conceived for long-term use in applications involving high operational temperatures and large temperature gradients such as that in aerospace.[5] Some of the potential FGM applications include coatings using graded composites of Mo-Si_3N_4,[6] cutting tools using WC-Co graded microstructure,[7] and functional gradient Ti-Co materials as dental implants.[8]

The FGM system based on Ti-TiB is of considerable interest for armor and ballistic applications.[9,10] This is based on the possibility that TiB, being a hard ceramic, can resist the penetration of high velocity projectiles and Ti, being a ductile metal, can serve as a backface containment structure. The interest in the Ti-TiB system is also because of the ease of fabrication of the gradation scheme due to the possibility of *in-situ* processing and the fact that TiB forms as whiskers and is very effective in stiffening and strengthening Ti.[11] Studies on composites based on low volume fraction TiB have demonstrated that superior mechanical properties can be attained, while the manufacturing processes can be economical.[12,13] However, the earlier fabrication trials of FGMs based on the Ti-TiB system had cracking problems,[14] partly owing to the low ductility of Ti-TiB composites. The Ti-TiB tiles cracked upon cooldown, with the fracture plane passing through one of the graded layers.[14] The objective of the present study is to synthesize crack-free Ti-TiB FGMs by ductilizing the matrix through the introduction of β-Ti phase by alloying. An *in-situ* reaction sintering approach is used to simultaneously form TiB whiskers and densify the FGM containing several composite layers. The microstructures, phase volume fractions, hardness levels, and residual stress have been determined in order to assess the suitability of this FGM for structural applications.

K.B. PANDA, Graduate Research Assistant, and K.S. RAVI CHANDRAN, Professor, are with the Department of Metallurgical Engineering, The University of Utah, Salt Lake City, UT 84112-0114. Contact e-mail: ravi@mines.utah.edu

Manuscript submitted August 2, 2002.

II. MATERIALS AND EXPERIMENTAL DETAILS

A. *Feasibility*

The phase diagram of the Ti-B system can be found elsewhere.[15] The Ti-B phase diagram has three compounds: TiB, Ti_3B_4, and TiB_2 at B compositions (wt pct) of 18 to 18.5, 22.4 pct, and 30.1 to 31.1 pct, respectively. There is some controversy with respect to the existence of Ti_3B_4 phase. Our earlier work[10,18] on Ti-TiB composites showed that TiB readily forms as whiskers upon reacting Ti with TiB_2. The work also confirms that no Ti_3B_4 phase was formed in any of the composites made, supporting one of the earlier works[16] questioning the existence of Ti_3B_4 phase. In the Ti-B system, the relevant reactions are

$$\mathrm{Ti} + \mathrm{B} \rightarrow \mathrm{TiB} \qquad [1a]$$

$$\mathrm{Ti} + 2\mathrm{B} \rightarrow \mathrm{TiB_2} \qquad [1b]$$

$$\mathrm{Ti} + \mathrm{TiB_2} \rightarrow 2\mathrm{TiB} \qquad [1c]$$

The free energy of formation of TiB and TiB_2 by the preceding reactions was calculated using standard thermodynamic data.[17] These data along with data for other Ti compounds are available elsewhere.[18] The data show that although the ΔG of formation of TiB_2 is the most negative, Ti and TiB_2 can further react to form TiB due to the small negativity of the free energy. This means that although TiB_2 can form first upon reacting B with Ti on the B-rich side, the TiB_2 will eventually be converted to TiB, as long as the average B concentration in the reaction zone is less than 18 to 18.5 pct. Although it is possible to retain TiB_2 by making the reaction incomplete, the interest here is to form graded composite layers with TiB whiskers in light of the fact that the amount of B required to form TiB is much less and the hardness of TiB is also very high (Vicker's hardness of about 1800 kgf/mm^2). In addition, TiB is known[10,18] to form as whiskers, which may be an advantage from the point of view of mechanical properties.

B. *Processing Approach for Ti-TiB FGM*

Powder processing techniques provide the flexibility desired for the fabrication of sound FGM composites.[19] For best reaction and densification, care must be taken at several steps such as the powder selection, mixing, and compaction, which largely influence the final microstructure and properties. In our previous work[18] on constant composition Ti-TiB composites, it was realized that tri-modal powder packing was necessary to achieve full density and uniform TiB distribution. Therefore, tri-modal powder packing that uses pure Ti powders, β-phase-stablizing elements, and TiB_2 powders was used to simultaneously form β-Ti matrix and TiB whiskers in the FGM layers.

The commercially available 99.95 wt pct Ti powders (α-Ti) (average particle size: 45 μm, composition in wt pct: 0.23O, 0.02N, 0.01C, 0.04Fe, and 0.024H) and TiB_2 powders (average particle size: 2 μm, composition in wt pct: 30.3B, 0.67Zr, 0.01C, 0.04Fe and 0.024H) were chosen. To stabilize the β-phase, Fe-Mo powders (average particle size: 10 μm, composition in wt pct: 59.8Mo) were used as the third powder. The tri-modal powder mixture had the size ratio 2:10:45, giving an initial packing density of about 92 pct. This is very close to the ideal size ratio of 1:7:49 for maximum packing of a tri-modal mixture.[20,21] Using this powder mixture, two sets of FGMs, one with five layers and another with six layers, were fabricated, and based on the solid-state reaction,

$$m\mathrm{Ti} + n(\mathrm{Fe\text{-}Mo}) + p\mathrm{TiB_2} \rightarrow x(\beta\text{-}\mathrm{Ti}) + y\mathrm{TiB} \qquad [2]$$

where m, n, and p are the mole fractions of the reacting species and x and y are the mole fractions of product species, β-Ti and TiB, respectively. By adjusting the relative proportions of reactants, different proportions of TiB in β-Ti matrix can be obtained. Tables I(a) and (b) illustrate the layer number, the targeted TiB vol pct, and the composition of the mixtures in wt pct in the different layers for both the FGMs. The level of β-equivalent for all the FGM layers was kept at 28 wt pct Mo. Hereafter, the six-layered and the five-layered fabricated tiles would be referred to as FGM1 and FGM2, respectively.

The different layers in the FGMs were stacked by pouring the powder mixtures blended for 24 hours in a graphite die and manually leveling them. Thin titanium foils (~0.033-mm thickness) were used in between the layers to prevent layer intermixing upon reaction sintering. The FGM layers were reaction sintered in a hot press at 1300 °C under a uniaxial pressure of 28 MPa in argon atmosphere for 2 hours. Microstructural characterization was done using the scanning electron microscope (SEM), Hitachi (Pleasanton, CA) S-3000N. The FGM layers were deep etched (etchant: Kroll's reagent) to reveal the microstructural features, especially the TiB whiskers. Phase analysis of the different layers was carried out by X-ray diffraction using a Siemens (Madison, WI) D5000 X-ray diffractometer. A Vickers hardness tester (LECO*, M-400) was used to measure the hardness levels of the FGM layers, under a load of 300 gf.

III. RESULTS

A. *Macrostructure*

Macrographs of the synthesized FGM plates are shown in Figures 1(a) and (b). It can be seen that a nearly uniform-layered structure has formed without delamination and residual porosity in FGM1. The layer interfaces were found to be sharp and strongly bonded. Although the layer boundaries are somewhat nonuniform in FGM2, the FGM was structurally as sound as FGM1. A detailed microstructure examination revealed that full density was achieved in all the layers. By careful control of powder stacking and leveling, it should be possible to obtain uniform layer thickness, but this was not a critical requirement in this research. Macroscopic examination did not reveal any cracks on the surface or in the interior of the FGMs. The absence of cracking is possibly due to the addition of β stabilizing elements to the Ti matrix in the layers.

B. *Microstructure*

Figures 2 through 6 illustrate the microstructure's various layers in FGM2. The low-magnification micrographs illustrate

---

*LECO is a trademark of LECO Corporation, Mahwah, NJ.

Table I. Compositions and Thicknesses of Layers in the FGMs

(a) FGM1

Layer	Target Vol Pct TiB	Composition of mixture (Wt Pct) Ti	Fe-Mo	TiB_2	Composition of mixture (Vol Pct) Ti	Fe-Mo	TiB_2	Thickness (mm)	Resulting Vol Pct TiB
1	0	82	18	0	90	10	0	5	0
2	10	81	16	3	87	10	3	3	12
3	20	78	16	6	84	9	7	3	23
4	30	75	15	10	81	9	10	3	34
5	40	70	15	15	76	8	16	3	43
6	50	67	13	20	71	8	21	4	52

(b) FGM2

Layer	Target Vol Pct TiB	Composition of mixture (Wt Pct) Ti	Fe-Mo	TiB_2	Composition of mixture (Vol Pct) Ti	Fe-Mo	TiB_2	Thickness (mm)	Resulting Vol Pct TiB
1	0	82	18	0	90	10	0	3.05	0
2	20	78	16	6	84	9	7	2.75	24
3	40	70	15	15	76	8	16	2.80	46
4	60	61	12	27	64	7	29	2.55	67
5	80	41	8	51	43	5	52	3.15	95

the microstructural uniformity, and the high-magnification ones provide details on the differing morphologies of primary and secondary TiB whiskers. Figures 2(a) and (b) illustrate the microstructure of the β-Ti layer. This microstructure is that of a typical β-Ti alloy, because of the high Mo-equivalent (28 wt. pct), caused by the Fe-Mo powder addition. The presence of grain boundary α as well as α-platelets nucleating within β-matrix can be seen (Figure 2(b)). There are also a few TiB whiskers, possibly due to the diffusion of B from the adjacent layer; however, their presence can be ignored for all practical purposes.

Figures 3(a) and (b) illustrate the microstructure of the Ti-24 vol pct TiB layer. The volume fraction of TiB in each layer was determined according to the procedure discussed in Appendix A. In this layer, first, there is a uniform distribution of TiB whiskers. The whiskers had an average length of about 15 μm and a width of about 1.5 μm (aspect ratio ~10). Second, the average size of the β grains seems to be significantly less relative to that in the β-Ti layer, possibly due to the presence of some TiB whiskers at β grain boundaries. Figures 4(a) and (b) illustrate the microstructures of the layer containing 46 vol pct TiB. Unlike that in the 24 vol pct TiB layer, one can see large colonies of agglomerated small TiB whiskers (Figure 4(b)) in addition to the primary TiB whiskers uniformly distributed in the β-Ti matrix. The average whisker length and width are about 10 μm and 0.75 μm (aspect ratio ~10), respectively, for the nonclustered primary whiskers, whereas they are about 2.5 and 0.5 μm (aspect ratio ~5), respectively, for the clustered regions. The clustered TiB regions appear porous because the β-Ti phase from regions between the whiskers was etched out to reveal the structure of the whiskers. The clustered regions are made of TiB and the residual β-Ti surrounding the TiB whiskers.

Figures 5(a) and (b) are the micrographs of the layer containing 67 vol pct TiB. Here, one can see a more pronounced formation of the clustered TiB morphology, compared to that seen in the 46 vol pct TiB layer. The average whisker length and width are about 7.5 and 0.5 μm (aspect ratio ~10), respectively, for the nonclustered primary TiB whiskers and about 2.5 and 0.5 μm (aspect ratio ~5), respectively, for the clustered regions. It should also be noted that the amount of primary TiB whiskers is very small in this layer. Figures 6(a) and (b) represent the microstructures for the last layer of the FGM plate containing approximately 95 vol pct TiB. This structure is an agglomerate of numerous TiB whiskers clustering together to form a nearly monolithic structure with some residual β-Ti between the whiskers. The average TiB whisker length and width are about 2.5 and 0.5 μm (aspect ratio ~5), respectively, in this layer. In addition, the layer demonstrates a structure that is quite close to the monolithic structure of TiB; the only difference here is the structure of the agglomerated tiny TiB whiskers. The "gaps" in the microstructure were filled by β-Ti, which was removed during the deep-etching performed to reveal the layer microstructure.

C. *X-Ray Diffraction Data*

Figure 7 shows the X-ray diffraction patterns of the individual layers of FGM2. The X-ray patterns indicate only the presence of Ti and TiB in the layers. This is in contrast to our previous study,[10] where some unreacted TiB_2 was round to be present at high TiB volume fractions. In our recent work,[18] however, we have shown that complete transformation of TiB_2 to TiB in β-Ti matrix can be accomplished with trimodal powder packing. The complete consumption of TiB_2 in the present study is probably due to the use of the size-optimized tri-modal packing of powders. In Figure 7, the dominant β-Ti peaks present are $(110)_{\beta\text{-Ti}}$, $(200)_{\beta\text{-Ti}}$, and $(211)_{\beta\text{-Ti}}$ and those for the TiB are $(200)_{\text{TiB}}$, $(201)_{\text{TiB}}$, $(210)_{\text{TiB}}$, $(102)_{\text{TiB}}$, $(312)_{\text{TiB}}$, and

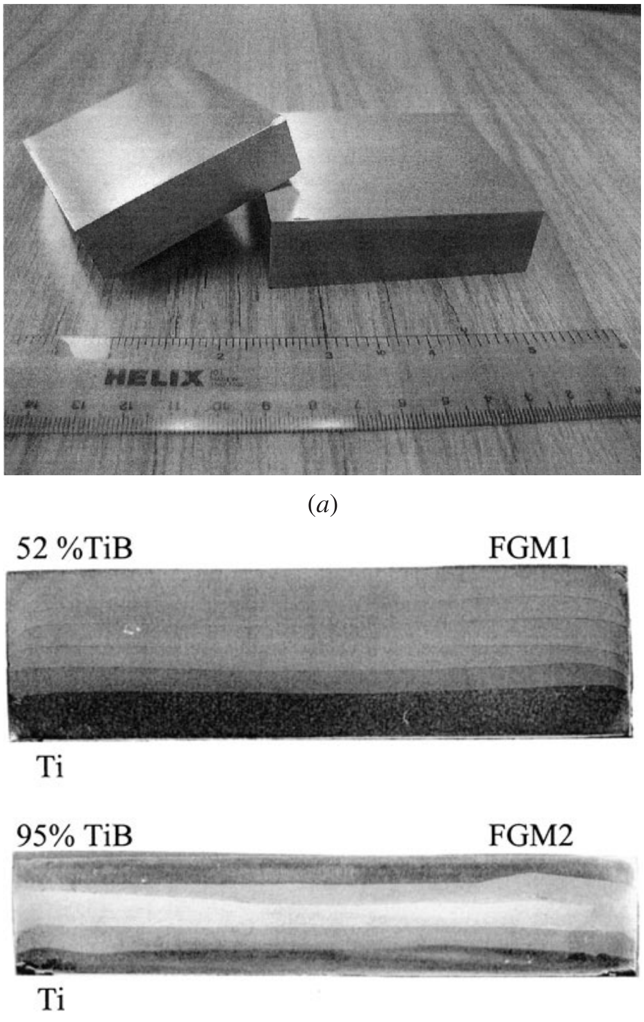

(*a*)

(*b*)

Fig. 1—Photographs of the FGMs synthesized in this study: (*a*) overall view and (*b*) polished and etched cross sections.

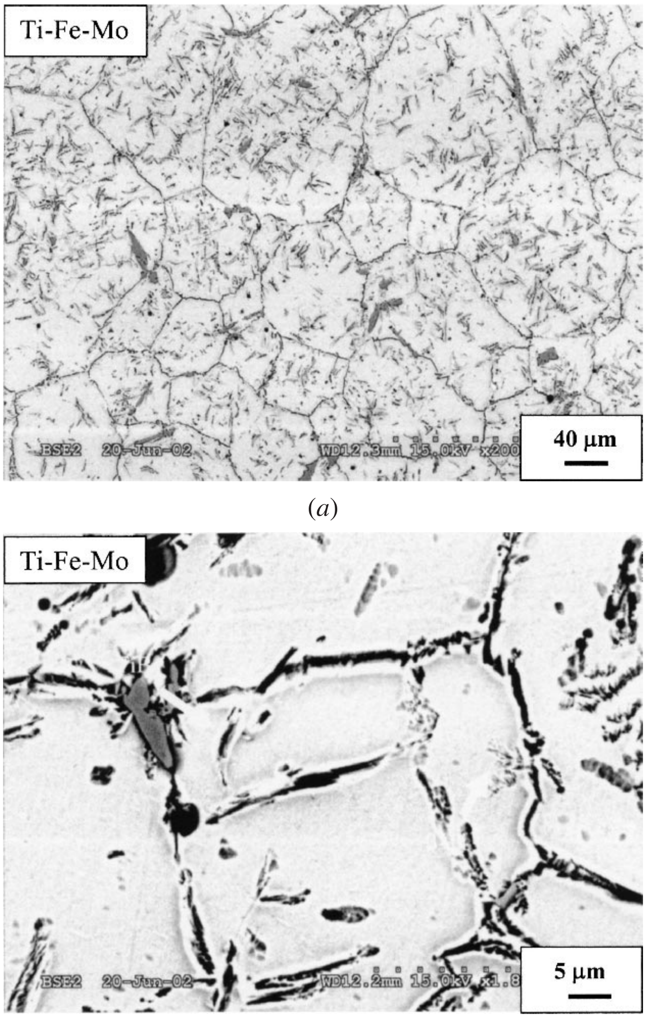

(*a*)

(*b*)

Fig. 2—SEM micrographs of the β-Ti layer in FGM2 taken at (*a*) low and (*b*) high magnifications.

$(122)_{TiB}$. In the FGMs, as one traverses the layers starting from the β-Ti side, the TiB volume fraction is increased. Therefore, it can be seen in Figure 7 that the intensity of the dominant β-Ti peaks decreased and that of the dominant TiB peaks increased as the volume fraction of TiB increased.

D. *Hardness*

The Vickers hardness profiles across the thickness for FGM1 and FGM2 are shown in Figures 8(a) and (b), respectively. The microhardness increased with the increase in the volume fraction of TiB in the layers. A maximum hardness value of about 740 Kgf/mm^2 was achieved in the layer containing 52 vol pct TiB in FGM1. Similarly, a maximum hardness value of about 1600 Kgf/mm^2 was observed in the case of the 95 vol pct TiB layer in FGM2. It is evident that for FGM1, the increase in hardness is gradual from the β-Ti layer to the opposite end containing 52 vol pct TiB layer. This is because we have a small and regular increase in the volume fraction of TiB in each layer, with about 10 vol pct TiB increment per layer. For FGM1, it seems that a 10 pct increase in vol pct TiB leads to an increase of about 15 pct in the hardness values, on the average. In the case of FGM2, it can be seen that the hardness variation is in steps. The layer-to-layer increase in the volume fraction of TiB in FGM2 is large (approximately 20 vol pct TiB) enough to lead to large jumps in hardness near the layer interfaces. However, there is a very large jump in the hardness between the fourth layer (67 vol pct TiB) and the fifth layer (95 vol pct TiB) in the case of FGM2. This jump is not in accordance with that in the previous layers partly because of the jump in the vol pct of TiB, which is about 30. The hardness value has approximately doubled between these layers. This could be due to the almost continuous phase structure of TiB (Figure 6), but a detailed analysis of this is beyond the scope of the present study.

E. *Residual Stress Distributions in the FGM*

Figures 9(a) and (b) show the residual stress distributions in FGM1 and FGM2, respectively. These stresses were calculated based on a one-dimensional elastic multilayer model, presented in Appendix B. The results indicate that the TiB-

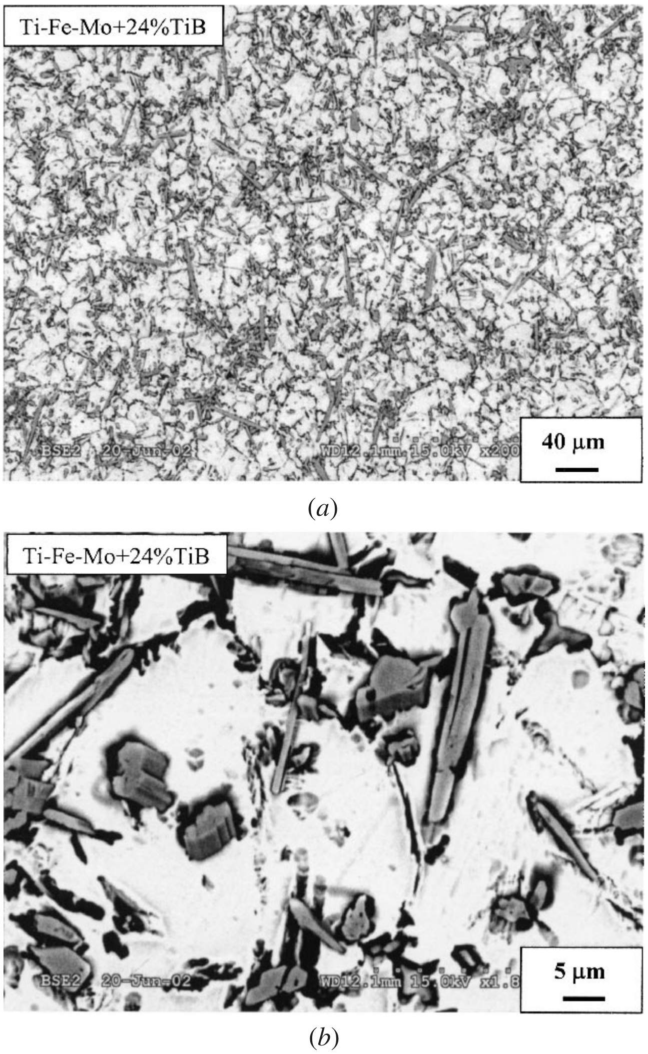

(*a*)

(*b*)

Fig. 3—SEM micrographs of the Ti-24TiB layer in FGM2 taken at (*a*) low and (*b*) high magnifications.

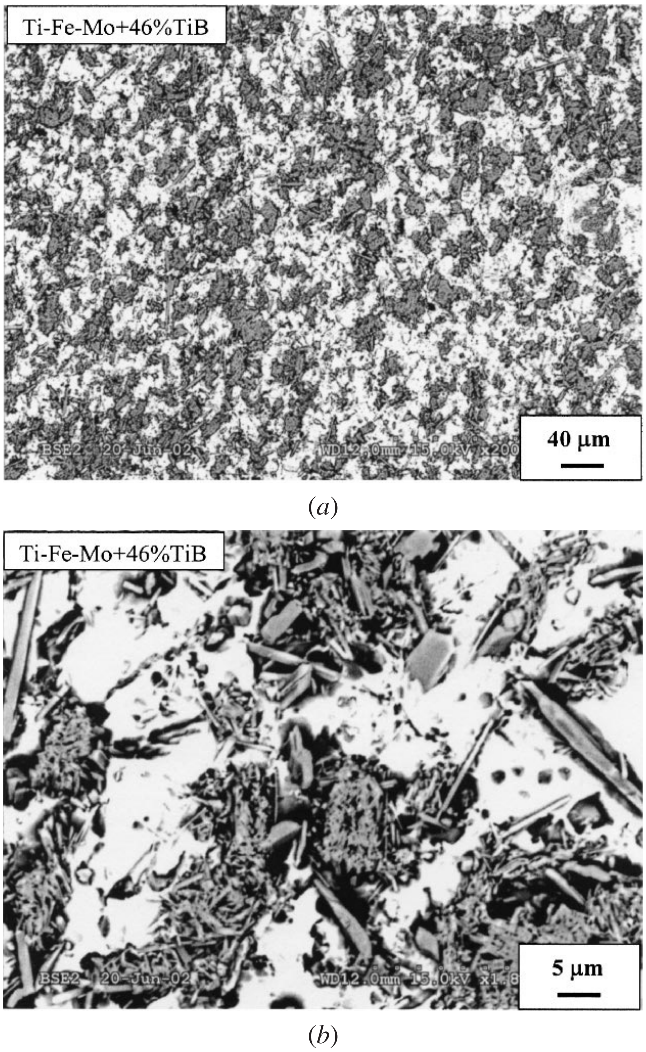

(*a*)

(*b*)

Fig. 4—SEM micrographs of the Ti-46TiB layer in FGM2 taken at (*a*) low and (*b*) high magnifications.

and Ti-rich regions are relatively in tension while the stresses in the layers having the two phases are generally compressive. The maximum values of the residual stresses in the TiB-rich layers in FGM1 and FGM2 are about 115 and 232 MPa, respectively. It is also noted that the outer layers are largely in tension, while the middle layers are relatively in compression satisfying the requirement that the net force across the FGM section should be zero. The tension in outer layers is caused by the nonuniformity of layer thickness, thus giving a nonlinear gradation profile in the macroscopic sense. If the layer thicknesses were uniform, a more symmetric stress distribution would result, as illustrated in our earlier work.[3] In FGM1, the CTE mismatch between the outer layers is relatively small and the variation in the CTE values across the thickness is also relatively less compared to that in FGM2. This gives rise to a relatively smaller magnitude of residual stress in FGM1. In the case of FGM2, owing to the large increments in the TiB volume fractions between the layers, there are relatively large differences in both the CTE values and the elastic properties between adjacent layers, and this gives rise to larger amplitudes in the residual stress distribution for FGM2. It is interesting to note that even though the residual stress reached a level of about 232 MPa in tension, the layer did not show any cracking*. This suggests that the TiB layer in the present FGM is structurally sound.

IV. DISCUSSION

A. *Effect of TiB Volume Fraction on the Microstructure*

The mechanism of TiB whisker formation with different morphologies at different volume fractions can be explained with the help of Figure 10. Our previous study[10] on reaction sintering between α-Ti and TiB_2 explained the microstructural morphologies in a bimodal powder packing arrangement. However, the question of how a similar TiB morphology is resulted in a β-matrix, with a trimodal powder mixture in this study, will be briefly explained.

---

*The average fracture strength of nearly 100 pct TiB material was determined[14] to be 262 MPa, and the tensile stresses in the FGMs are lower than this value.

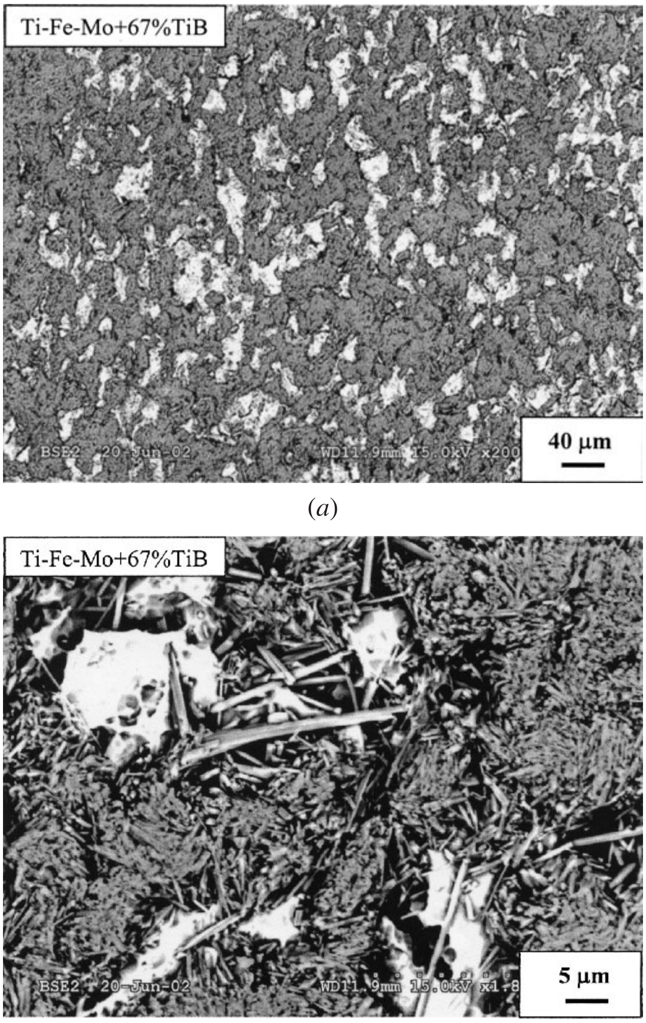

(*a*)

(*b*)

Fig. 5—SEM micrographs of the Ti-67TiB layer in FGM2 taken at (*a*) low and (*b*) high magnifications.

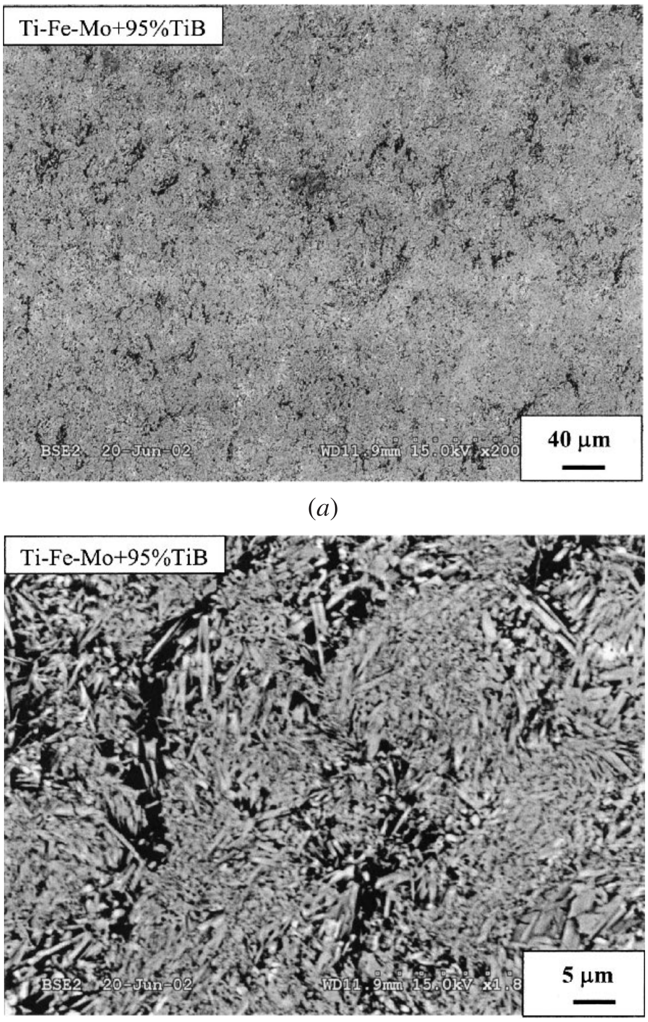

(*a*)

(*b*)

Fig. 6—SEM micrographs of the Ti-95TiB layer in FGM2 taken at (*a*) low and (*b*) high magnifications.

In the case of the layer with TiB volume fraction below about 30 vol pct TiB, the idealized equilibrium particle arrangement for Ti, Fe-Mo, and TiB_2 particles is likely to be as in Figure 10(a). The TiB_2 particles, owing to their very small sizes (2 μm), would go into the interstices between the large Ti (45 μm) particles and the Fe-Mo particles (10 μm). The mean free path (MFP) for TiB growth in Ti will be of the order of Ti particle size. Growth of the TiB whiskers, into the β-Ti particles, can proceed (Figure 10(b)) until complete decomposition of TiB_2 occurs. Thus, we observe high aspect ratio TiB whiskers, isolated from each other (Figures 2(a) and (b)).

In the case of a layer having 46 vol pct TiB, there are likely to be more TiB_2 particles between Ti and Fe-Mo particles, in the equilibrium packing configuration (Figure 10(c)). Here, while a few primary TiB whiskers will grow unimpeded (Figure 10(d)) in Ti particles, a substantial fraction of TiB_2 are not in direct contact with Ti, thus relying on backward diffusion of Ti into TiB_2 regions for TiB formation. This requirement, as explained in detail in our earlier study[10] will lead to the formation of secondary TiB whiskers from TiB_2 particles. This is largely due to the very small diffusivity rates of B in the transverse direction (the diffusivity values of B in the axial direction of TiB at 1300 °C was estimated to be 2.082×10^{-12} m/s and that in the transverse direction is several times smaller[22]). The microstructural features in Figures 4(a) and (b) are consistent with this mechanism.

In the high volume fraction layers (67 and 95 vol pct TiB), more TiB_2 particles surround the Ti particles and this leads to even further reduction in the number of particles in direct contact with Ti particles (Figure 10(e)). This again requires the backward diffusion of Ti into the TiB_2 region for TiB formation, leading to the formation of numerous short TiB whiskers, connected to each other,[10] and a few, thin primary TiB whiskers, as illustrated in Figure 10(f). The microstructural features in Figures 5(b) and 6(b) for the 67 and 97 pct TiB layers, respectively, are consistent with this mechanism.

It should be noted that the presence of Fe-Mo does not seem to alter the mechanism of formation of TiB. This is evident when the microstructural features of this work are compared with those in our earlier study,[10] which did not

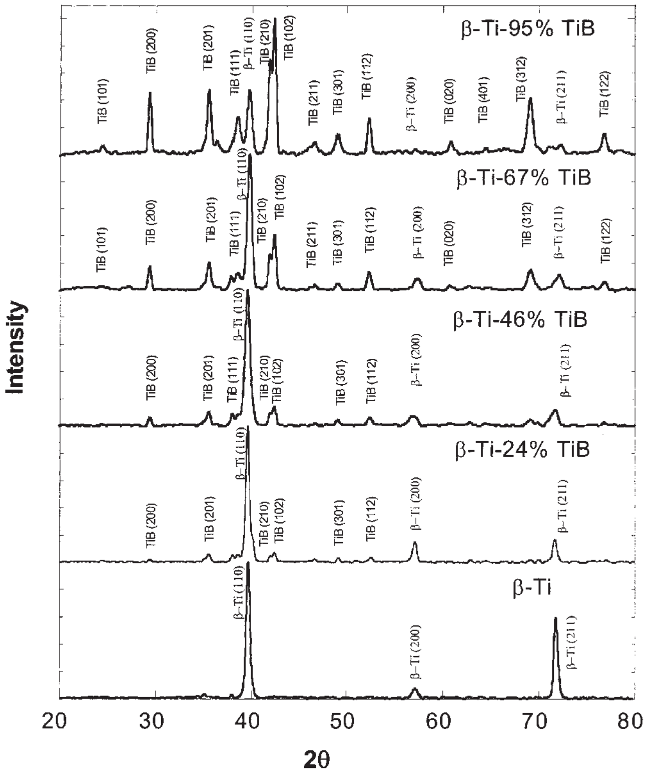

Fig. 7—X-ray diffraction patterns of different layers in FGM2.

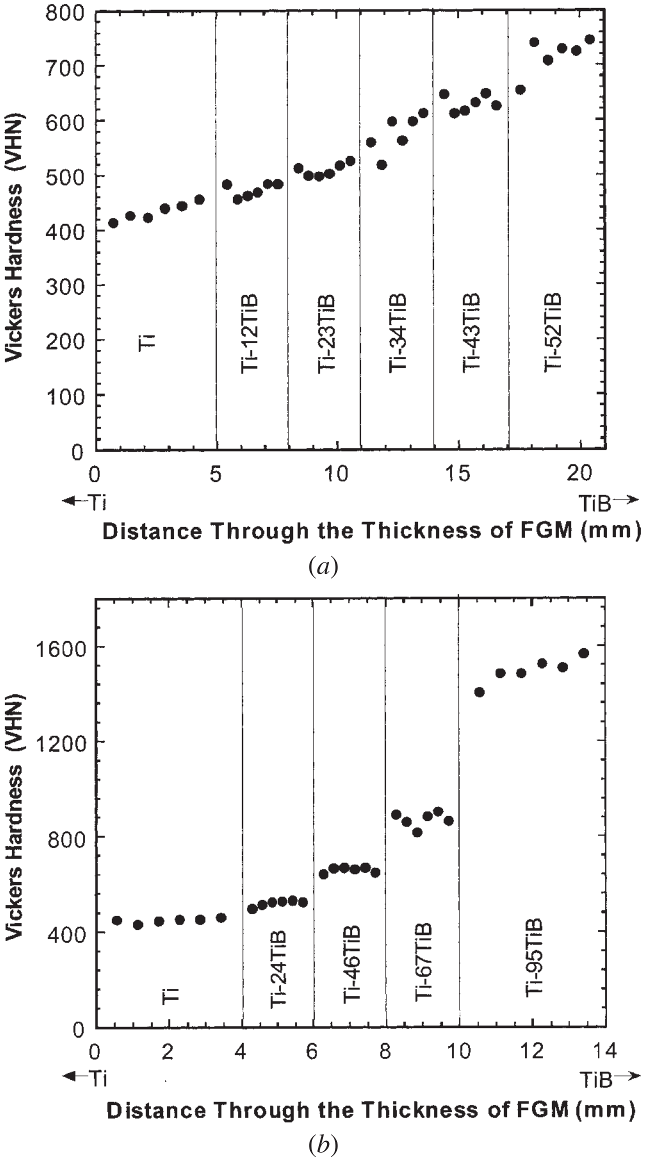

Fig. 8—The variation in the Vickers microhardness levels across the thickness of Ti-TiB layers in (*a*) FGM1 and (*b*) FGM2.

use the Fe-Mo particles and the trimodal powder packing arrangement.

B. *Hardness Variation Across the FGMs*

The increase in hardness across the layers is consistent with the increase in the volume fraction of hard TiB whiskers. The Vickers' hardness of TiB is about 1800 Kgf/mm^2, while that of TiB_2 varies from 2500 to 3000 Kgf/mm^2.[23,24] The residual stress is tensile in the surface regions of TiB-rich layer, and this may explain the relatively lower hardness of the TiB-rich layer (1600 Kgf/mm^2) in FGM2. Although the hardening of FGM with TiB is relatively less effective compared to TiB_2, the reasonable hardness of the TiB-rich layer (1600 Kgf/mm^2), the relatively lower amount of B required, and the one-shot nature of the processing suggest that the present FGM concept may be very viable for engineering applications.

V. CONCLUSIONS

1. The concept of reaction sintering to synthesize the TiB whiskers *in situ* was successful in producing dense, crack-free functionally graded materials, with a good adhesion between layers. The complete transformation of the TiB_2 into TiB in a β-Ti matrix, with a uniform and homogeneous reinforcement structure, was also achieved in one-step operation.
2. The morphologies of TiB whiskers varied according to the TiB volume fraction. At low TiB volume fractions, long primary whiskers were formed. At intermediate TiB volume fractions, a dual TiB morphology comprising primary TiB as well as short, clustered TiB was formed. At high volume fractions, all the TiB was in the form of short clusters. These variations could be explained on the basis of the mean-free-path available for the growth of TiB whiskers from the TiB_2 particles, as well as the nature of diffusion of B in TiB and backward diffusion of Ti in TiB_2.
3. The X-ray direct comparison method, based on the analysis of integrated intensities of β-Ti and TiB phases, was successfully used to determine the volume fractions of TiB whiskers in the FGM layers. This may be useful for the FGMs with multiple phases and when the other methods such as optical microscopy may be less reliable.
4. The hardness increased from a value of 420 kgf/mm^2 at the β-Ti surface layer to a value of 1600 kgf/mm^2 at the 95 vol pct TiB surface layer, indicating about 4 times increase in hardness from one side to the other. While the variation in hardness was smooth in the FGM with

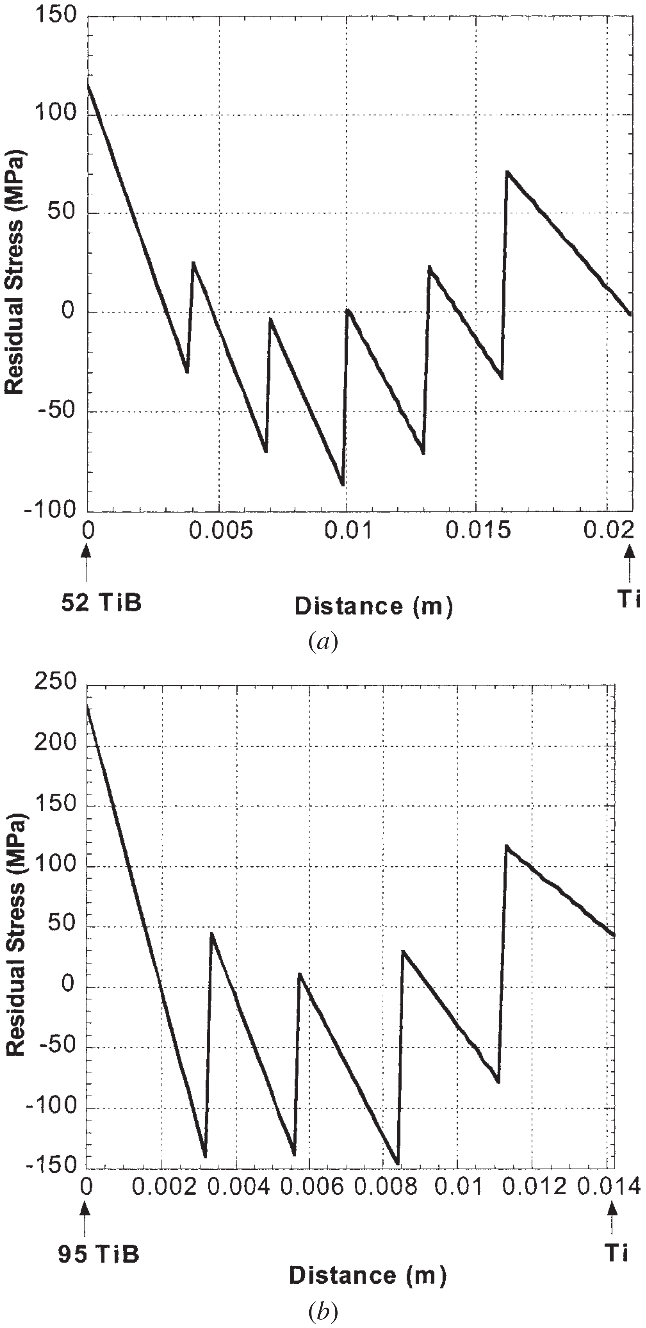

(*a*)

(*b*)

Fig. 9—The residual stress levels calculated from Eq. [B7] for (*a*) FGM1 and (*b*) FGM2.

52 pct TiB as the maximum, the variation was sharp across the interfaces in the FGM with 95 pct TiB as the maximum TiB volume fraction.

5. Based on a simple mechanics-of-materials-based theory, the residual stress distribution in the FGM was determined. The results revealed that although the overall residual stress levels are low, the top surface TiB-rich layers were in tension. In the highly graded Ti-TiB FGM, the TiB surface stresses were about 232 MPa in tension. Nevertheless, the TiB layer did not show any cracking, attesting to the structural soundness of the FGM.

ACKNOWLEDGMENTS

This research was supported by Grant No. DAAL19-99-1-0281 from the Army Research Office (Research Triangle Park, NC) The authors thank the program manager, Dr. David Stepp, Army Research Office, for the support and interest.

APPENDIX A

Determination of volume fraction of TiB in the FGM layers

The volume fractions of TiB in the layers were determined from the integrated intensities of peaks in the X-ray diffraction patterns according to the direct comparison method.[25] The details of this procedure are described elsewhere.[10] Here, we present a brief description of the determination of the structure factor, F_{hkl}, and the unit cell volume, V_0, for β-Ti, which is influenced by the Fe and Mo atoms in Ti lattice. In β solid solution, the β-stabilizing elements substitute randomly in the Ti lattice. With the lack of a better approach, the rule of mixtures was applied to determine the average atomic scattering factor, on the basis of the assumption that the solid solution was completely random and free of ordering. Thus, for β-Ti alloyed with Fe and Mo, the average scattering factor (f_{av}) can be written as

$$f_{av} = X_{\mathrm{Ti}} f_{\mathrm{Ti}} + X_{\mathrm{Fe}} f_{\mathrm{Fe}} + X_{\mathrm{Mo}} f_{\mathrm{Mo}} \qquad \text{[A1]}$$

where X_{Ti}, X_{Fe}, and X_{Mo} are the atomic fractions, and f_{Ti}, f_{Fe}, and f_{Mo} are the atomic scattering factors for Ti, Fe, and Mo atoms, respectively. The structure factor corresponding to the β-Ti composition in the present work was then calculated from f_{av}. These values are given in Table AI. A lattice parameter value of 3.2242 Å was used to calculate the β-Ti unit cell volume.

Table AI. Normalized Integrated X-Ray Line Intensities for the β-Ti Peaks

hkl	2θ	*d* (A)	$\lvert F\rvert^2$	*L*	*p*	I_c of β-Ti	I_β-Ti in JCPDS	I_β-Ti in β-Ti	I_β-Ti in β-Ti-24TiB	I_β-Ti in β-Ti-46TiB	I_β-Ti in β-Ti-67TiB	I_β-Ti in β-Ti-95TiB	*R*
110	38.48	2.33	1093	16	12	100	100	100	100	100	100	100	183.9
200	55.54	1.65	793	7	6	16	12	9	15	15	10	8	29.11
211	69.60	1.34	652	4	24	32	17	12	17	17	11	12	58.44
220	82.44	1.16	556	3	12	10	4	4	4	3	4	4	18.49
310	94.92	1.04	487	3	24	15	5	—	—	—	—	—	28.55
222	107.6	0.95	431	3	8	5	1	—	—	—	—	—	8.703

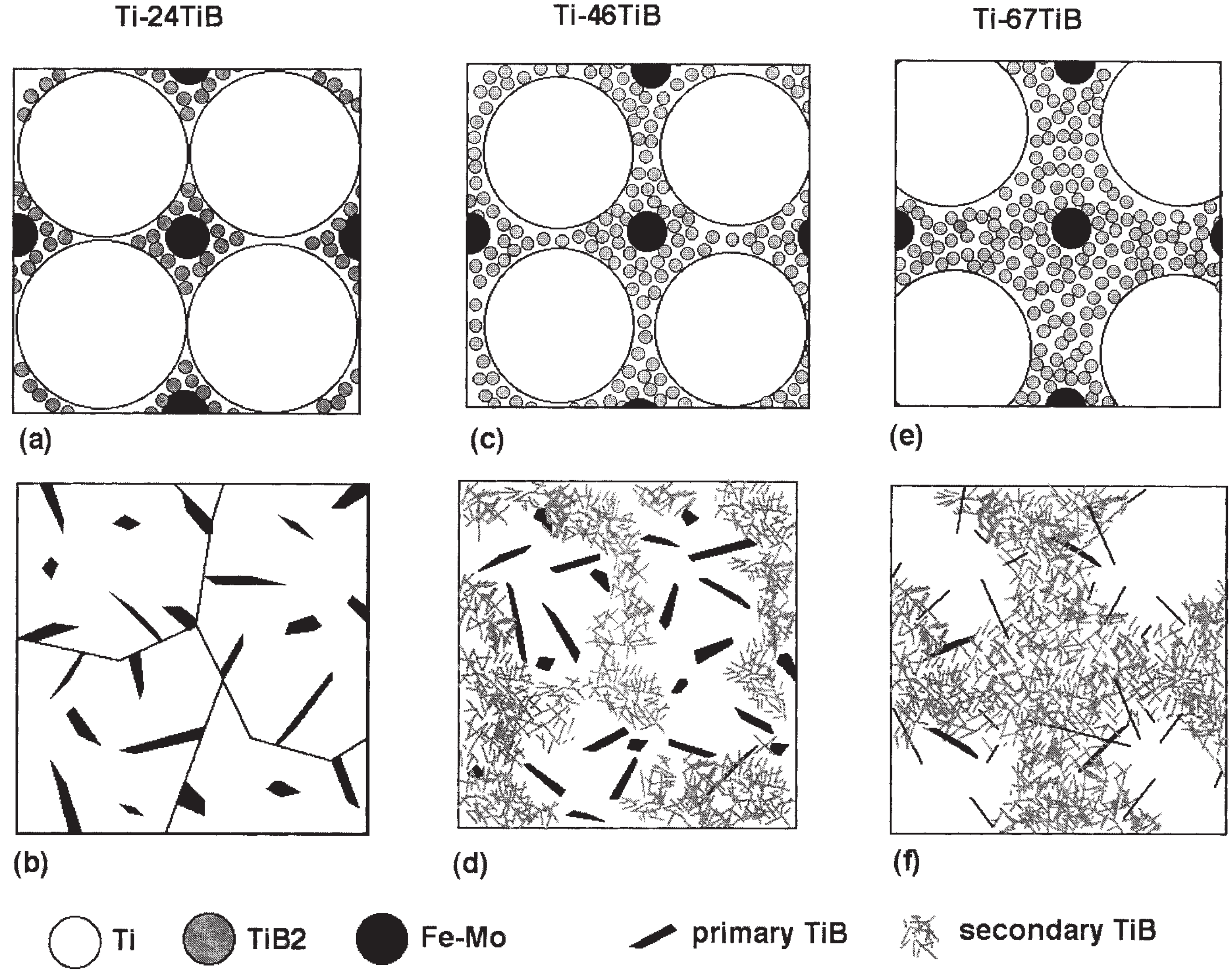

Fig. 10—Schematic describing the development of TiB whisker morphologies in Ti-TiB FGM layers: (*a*), (*c*), and (*e*) illustrate the trimodal powder packing for the FGM layers containing 7, 16, and 29 vol pct TiB_2 in the starting mixtures, respectively, and (*b*), (*d*), and (*f*) show the resulting morphologies of TiB whiskers.

The procedure used for TiB volume fraction estimation was almost the same as in our previous work,[10] except that the integrated intensities for the β-Ti from Table AI were used. To determine the TiB volume fractions in the FGM layers, the X-ray peaks considered in the calculations were $(110)_{\beta\text{-Ti}}$, $(200)_{TiB}$, $(201)_{TiB}$, and $(112)_{TiB}$. Table I in the main text shows the TiB volume fractions thus estimated for the layers present in the FGMs. It is evident that the targeted and the actual volume fractions agree reasonably well for both the FGMs.

APPENDIX B

Analytical Modeling of Residual Stress

Because the FGMs have varying volume fractions of TiB through the thickness, build up of residual stresses inside the FGM after cooling from high temperature can be expected. The room-temperature coefficient of thermal expansion (CTE) of the TiB-rich layer (95 vol pct) is about 38 pct lower than that of β-Ti. This difference in the CTE values can lead to some level of residual stresses, particularly at the interfaces of the layers. Therefore, it was considered important to estimate the residual stresses in the FGM layers. It is assumed that the residual stresses are generated under elastic conditions during cooldown, which is a reasonable approximation.

Residual stresses after cooling a FGM system involve two principal contributions, one arising from stress equilibrium due to differential contraction of layers and the other coming from the moment due to asymmetric stress distribution.[26] The latter arises from the asymmetric variations in the proportions of the constituents, and hence the elastic and thermal expansion characteristics, across the FGM thickness. The residual stresses arising from these two effects can be calculated with a good level of accuracy using a simple beam theory developed earlier[3] for FGMs with continuous variation of CTE and E across the thickness. That theory was based on the approach suggested by Timoshenko and Goodier[26] to calculate the thermal stresses in structures. Here, that approach is modified for FGMs containing discrete layers each with constant composition.

If, for instance, an infinitely long FGM plate having unit dimension in depth is considered to cool down through a temperature differential ΔT after processing at high temperature, the β-Ti-rich layers would contract more than the TiB-rich layers. However, if the plate is fixed along the edges and in addition if the out-of-plane bending is prevented (Figure B1), tensile stresses opposing these contractions would develop in the plate, due to the edge restraints. These tensile stresses, σ_i, would vary depending on the layer properties and are given by

$$\sigma_i = \alpha_i E_i \Delta T \qquad \text{[B1]}$$

where α_i and E_i are the CTE and E values of the ith layer. However, this edge restraint is not realistic for a freely shrinking FGM plate; therefore, the restraint should be mathematically removed by the superposition of an equivalent and opposite force. This force, F, is given by*

$$F = -\sum \alpha_i E_i (b_i - b_{i-1}) \Delta T \qquad \text{[B2]}$$

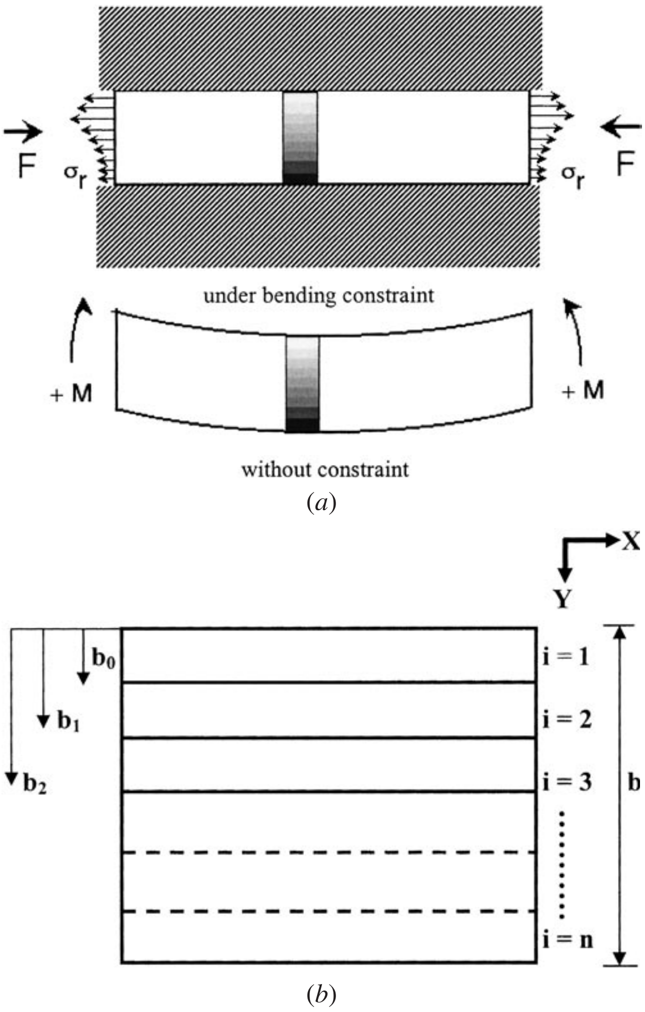

Fig. B1—A schematic of (*a*) the layer arrangement and (*b*) the FGM with and without bending constraint

where b_i and b_{i-1} are the distances of the layer interfaces between the ith and $(i + 1)$th layer, with the surface layer $(i = 1)$ of the plate located at b_0, as illustrated in Figure B1(b). The summation in Eq. [B2] is taken over all the layers. This force is equivalent to the application of stress in individual layers, as given by

$$\sigma_i = -E_i \frac{\sum \alpha_i E_i (b_i - b_{i-1}) \Delta T}{\sum E_i (b_i - b_{i-1})} \qquad \text{[B3]}$$

Therefore, the total stress in the absence of bending is the sum of Eq. [B1] and [B3] and is given by

$$\sigma_t = \left(\alpha_i E_i - E_i \frac{\sum \alpha_i E_i (b_i - b_{i-1})}{\sum E_i (b_i - b_{i-1})}\right) \Delta T \qquad \text{[B4]}$$

Equation [B4] implies that the FGM remains straight and therefore the stresses are applicable only when the bending of FGM during cooldown is prevented by some constraint (Figure B1(a); top). However, in reality, the freely shrinking FGM is not subjected to any constraint and must be allowed to bend (Figure B1(a); bottom), due to the asymmetric nature of stresses from Eq. [B4] through the thickness of the plate. Therefore, the actual stresses in the FGM plate are the stresses in equilibrium after the removal of the bending constraint. Following the mechanics of materials principles,[27] the bending stresses can be computed from the moment generated by the asymmetric stress distribution (Eq. [B4]) itself. The bending stresses are then to be added to Eq. [B4] to determine the actual total residual stress distribution in the FGM plate. The net moment generated by the asymmetric contraction stresses is thus given by[28]

$$M_t = \sum \left\{ \left[\alpha_i E_i \Delta T - E_i \frac{\sum \alpha_i E_i (b_i - b_{i-1}) \Delta T}{\sum E_i (b_i - b_{i-1})} \right] \left[\frac{b_i^2 - b_{i-1}^2}{2} \right] \right\} \qquad \text{[B5]}$$

The stresses generated by this moment are then given by

$$\sigma_i^b(y) = \left[\frac{6E_i M_t \left[2\sum (b_i - b_{i-1}) E_i . y - \sum (b_i^2 - b_{i-1}^2) E_i \right]}{4\left[\sum (b_i - b_{i-1}) E_i . \sum (b_i^3 - b_{i-1}^3) E_i \right] - 3\left[\sum (b_i^2 - b_{i-1}^2) E_i \right]^2} \right] \qquad \text{[B6]}$$

Then, the total residual stresses are given by the addition of normal (Eq. [B4]) and moment-induced stresses (Eq. [B6]):

$$\sigma_i^{\text{res}}(y) = \left[\alpha_i E_i \Delta T - E_i \frac{\sum \alpha_i E_i (b_i - b_{i-1}) \Delta T}{\sum E_i (b_i - b_{i-1})} \right] + \frac{6E_i M_t \left[2\sum (b_i - b_{i-1}) E_i . y - \sum (b_i^2 - b_{i-1}^2) E_i \right]}{4\left[\sum (b_i - b_{i-1}) E_i . \sum (b_i^3 - b_{i-1}^3) E_i \right] - 3\left[\sum (b_i^2 - b_{i-1}^2) E_i \right]^2} \qquad \text{[B7]}$$

The accuracy of Eq. [B7] was verified through the finite-element analysis of a bimaterial.[14]

For the calculation of residual stresses in the FGMs, the CTE values for Ti and TiB at room temperature were taken as 10×10^{-6}/°C and 6.2×10^{-6}/°C, respectively, based on

---

*Since we consider unit width in the one-dimensional modeling, the units of force will have to come out to be N/m; however, this is N for unit-width material.

Table BI. The Calculated Elastic Moduli and the Coefficients of Thermal Expansion Data for the Layers in the FGMs

(a) FGM1

Layer	Thickness (mm)	E (GPa)	α (CTE) (/°C)
1	5	75	10.0×10^{-6}
2	3	97	8.96×10^{-6}
3	3	118	8.28×10^{-6}
4	3	142	7.77×10^{-6}
5	3	164	7.43×10^{-6}
6	4	187	7.15×10^{-6}

(b) FGM2

Layer	Thickness (mm)	E (GPa)	α (CTE) (/°C)
1	3.05	75	10.0×10^{-6}
2	2.75	121	8.23×10^{-6}
3	2.80	171	7.33×10^{-6}
4	2.55	231	6.78×10^{-6}
5	3.15	344	6.27×10^{-6}

our previous research and literature.[14,29] The CTE values of the layers were calculated according to Turner's equation[30] for particulate-reinforced composites:

$$\alpha_c = \frac{\alpha_m V_m K_m + \alpha_p V_p K_p}{V_m K_m + V_p K_p} \qquad \text{[B8]}$$

where α_m and α_p, V_m and V_p, and K_m and K_p are the CTE values, the volume fractions, and the bulk moduli of the matrix (β-Ti) and the particle (TiB), respectively. The elastic moduli for the different layers were calculated using the Halpin–Tsai (H–T) equation.[31,32] Tables BI(a) and (b) show the calculated values of CTE and E for the different layers of FGM1 and FGM2, respectively. The elastic moduli of the layers were calculated by taking the moduli of β-Ti and TiB as 75 and 371 GPa, respectively.[11,29] The aspect ratio of fibers (TiB Whiskers) was taken to be 7.5 in these calculations. From our previous work,[11] it was found that this aspect ratio adequately explained the changes in elastic modulus with TiB volume fraction, even though some of the microstructure consisted of bimodal TiB distribution. We assume here that the same situation applies to thermal expansion behavior and thus felt justified using 7.5 as the aspect ratio.

REFERENCES

1. R. Watanabe, A. Kawasaki, and H. Takahashi: in *Mechanics and Mechanisms of Damage in Composites and Multi-Materials,* D. Baptiste, ed., Mechanical Engineering Publications, London, 1991, pp. 285-99.
2. K. Ichikawa: *Functionally Graded Materials in the 21st Century,* Kluwer Academic Publishers, Dordrecht, The Netherlands, 2001, pp. 64-69.
3. K.S. Ravichandran: *Mater. Sci. Eng.,* 1995, vol. A201, pp. 269-76.
4. A.E. Giannakopoulos, S. Suresh, M. Finot, and M. Oisson: *Acta Metall. Mater.,* 1995, vol. 43, pp. 1335-44.
5. M. Koizumi: *Ceram. Trans.,* 1992, vol. 34, pp. 1-10.
6. B. Sauhan, W. Luxem, M. Bartsch, M. Schmucker, and H. Schneider: *Materials Science Forum,* Proc. 5th Int. Symp. on Functionally Gradient Materials, Trans Tech Publications, Uetikonzuerich, Switzerland, 1999, vol. 308–311, pp. 47-52.
7. P. Nicolae: *Materials Science Forum,* Proc. 5th Int. Symp. on Functionally Gradient Materials, Trans Tech Publications, Uetikonzuerich, Switzerland, 1999, vols. 308–311, pp. 482-86.
8. F. Watari, A. Yokoyama, H. Matsuno, F. Saso, M. Uo, and T. Kawasaki: *Materials Science Forum,* Proc. 5th Int. Symp. on Functionally Gradient Materials, Trans Tech Publications, Uetikonzuerich, Switzerland, 1999, vol. 308–311, pp. 356-61.
9. W.A. Gooch, M.S. Burkins, R. Palicka, J. Rubin, and K.S. Ravichandran: *Materials Science Forum,* Proc. 5th Int. Symp. on Functionally Gradient Materials, Trans Tech Publications, Uetikonzuerich, Switzerland, 1999, vols. 308–311, pp. 614-21
10. S.S. Sahay, K.S. Ravi Chandran, R. Atri, B. Chen, and J. Rubin: *J. Mater. Res.,* 1999, vol. 14, pp. 4214-23.
11. R.R. Atri, K.S. Ravichandran, and S.K. Jha: *Mater. Sci. Eng.,* 1999, vol. A271, pp. 150-59.
12. A. Fan, P. Midownik, L. Chandrasekaran, and M. Ward-close: *J. Mater. Sci.,* 1994, vol. 29, pp. 1127-34.
13. W.O. Soboyejo, R.J. Lederich, and S.M.L. Sastry: *Acta Metall. Mater.,* 1994, vol. 42, pp. 2579-91.
14. R.R Atri: Ph.D. Thesis, University of Utah, Salt Lake City, UT 2000.
15. *ASM Handbook: Alloy Phase Diagrams,* H. Baker, ed., ASM INTERNATIONAL, Materials Park, OH, 1992, vol. 3, pp. 2-85.
16. K.E. Spear, P. McDowell, and F. McMohan: *J. Am. Ceram. Soc.,* 1986, vol. 69, pp. C-4-C-6.
17. *HSC Chemistry for Windows,* Ver. 1.10, Chemical Reaction and Equilibrium Software, A. Roine, ed., Outkumpu Research Oy, Pori, Finland, 1993.
18. K.B. Panda and K.S. Ravi Chandran: *Metall. Mater. Trans.* A, 2003, vol. 34A, pp. 1371-85.
19. U. Leushake, A.N. Winter, B.H. Rabin, and B.A. Corff: *Materials Science Forum,* Proc. 5th Int. Symp. on Functionally Gradient Materials, Trans Tech Publications, Uetikonzuerich, Switzerland, 1999, vols. 308–311, pp. 13-18.
20. R.M. German: *Powder Metallurgy Science,* 2nd ed., MPIF, Princeton, NJ, 1994, p. 166.
21. R.M. German: *Powder Packing Characteristics,* MPIF, Princeton, NJ, 1994, p. 183.
22. Z. Fan, Z.X. Guo, and B. Cantor: *Composites,* 1997, vol. 28A, pp. 131-40.
23. R.G. Munro: *J. Res. Nat. Inst. Stand. Technol.,* 2000, vol. 105, pp. 709-20.
24. H. Itoh, S. Naka, T. Matsudaira, and H. Hamamoto: *J. Mater. Sci.,* 1990, vol. 25, pp. 533-36.
25. B.D. Cullity: *Elements of X-Ray Diffraction,* 2nd ed., Addison-Wesley, Reading, MA.
26. P. Timoshenko and J.N. Goodier: *Theory of Elasticity,* 3rd ed., Mc-Graw-Hill, New York, NY, 1970, p. 433.
27. M. Gere and S.P. Timoshenko: *Mechanics of Materials,* 4th ed., PWS Publishing Co., Boston, MA, 1997, p. 57.
28. S.G. Lekhnitskii: *Anisotropic Plates,* translated from 2nd Russian edition, Gordon and Breach, New York, NY, 1968, pp. 74-84.
29. K. Wang, L. Gustavson, and J. Dumbleton: in *Beta Titanium Alloys in the 1990's,* D. Eylon, R.R. Boyer, and D.A. Koss, eds., TMS, Warrendale, PA, 1993, p. 49-60
30. D.K. Balch, T.J. Fitzerald, V.J. Michaud, A. Mortensen, Y.L. Shen, and S. Suresh: *Metall. Mater. Trans.,* A, 1996, vol. 27A, pp. 3700-13.
31. K.S. Ravichandran: *J. Am. Ceram. Soc.,* 1994, vol. 77, pp. 1178-84.
32. P.K. Mallick: *Fiber-Reinforced Composites: Materials Manufacturing and Design,* Marcel Decker, Inc., Princeton, NJ, 1988, p. 129.